Rock Mechanics and Rock Engineering (2020) 53:3111–3131
https://doi.org/10.1007/s00603-020-02094-3

ORIGINAL PAPER

Comparative Investigation on the Compression–Shear and Tension–Shear Behaviour of Sandstone at Different Shearing Rates

Da Huang[1] · Duofeng Cen[1] · Yixiang Song[1]

Received: 8 March 2019 / Accepted: 24 March 2020 / Published online: 2 April 2020

Abstract
Direct shear tests on rocks under compression–shear stress conditions have been widely conducted, whereas few have been performed under tension–shear stress conditions. However, rocks exhibit tension–shear failures in many scenarios, such as in the excavation disturbed zone in deep underground caverns and high slopes. A series of direct shear tests were performed with cuboid sandstone specimens under different normal tensile stresses ($\sigma_n = -3$, -2, and -1 MPa) and compressive stresses ($\sigma_n = 1$, 3, and 5 MPa) at different shearing rates ($v = 0.2$, 1, 5, and 10 mm/min). The tension–shear tests were performed using an auxiliary device in combination with a compression–shear testing machine. The results showed that the fracture, shear stress–displacement curve, shear stiffness and shear strength were affected by both σ_n and v, and the differences in these mechanical behaviour between compression–shear and tension–shear cases were analysed in detail. The shear strength had a nonlinear relationship with both σ_n and v in the full region of tested normal stress (namely, the normal stress range from tension to low compression). The Hoek–Brown criterion ($\tau = A(\sigma_n - \sigma_t)^B$) considering the shearing rate effect (the relationship between parameter A (B) and shearing rate v is represented by a natural logarithm function) was proposed as the optimal shearing rate-dependent strength criterion for sandstone in the tested normal stress range.

Keywords Compression–shear · Tension–shear · Hoek–Brown strength criterion · Shearing rate

List of Symbols

σ_n	Normal stress
σ_t	Tensile strength
σ_{cc}	Crack closure stress
σ_{ci}	Crack initiation stress
σ_{cd}	Crack damage stress
τ	Shear strength
τ'	Residual shear strength
v	Shearing rate
φ	Internal friction angle
c	Cohesion
φ'	Residual friction angle
$k_{elastic}$	Shear stiffness in the elastic deformation stage
$k_{average}$	Pre-peak average shear stiffness
μ	Coefficient of friction on the crack face
σ_c'	Critical macroscopic compressive stress needed for closing the crack
m	Material constant of Hoek–Brown criterion
A, B	Fitting parameters of Hoek–Brown criterion

1 Introduction

As rocks are generally in a compressive stress state, the compression/shear properties of rocks under confining/normal pressure have been widely studied (Petit 1988; Wibberley et al. 2000; Cho et al. 2008; Cai and Liu 2009; Chen et al. 2016; Peng et al. 2016; Turichshev and Hadjigeorgiou 2016; Yang 2016). Most of the strength criteria in the rock mechanics field were derived on the basis of compression–shear failure (Haimson and Bobet 2012). In fact, tensile stress in rocks is a very common phenomenon in the Earth's crust, such as in the rocks near a folding centre or fault wall (Ferrill et al. 2012), in the unloading zone induced by engineering excavation or river incision (Cen and Huang 2017; Cen et al. 2020) and in slopes subjected to earthquakes (Huang et al. 2019). For instance, the rocks in the excavation disturbed

✉ Duofeng Cen
duofengcen@hebut.edu.cn

[1] School of Civil and Transportation Engineering, Hebei University of Technology, Tianjin 300401, China

zone (EDZ) of underground openings, especially those that are deeply buried, and high slopes are usually under composite tension–compression stress conditions (Goodman 1989; Aimone-Martin et al. 1997; Huang et al. 2001; Huang and Huang 2014) due to differential rebounding deformation in the process of stress redistribution (Wu et al. 2009; Huang and Huang 2014), where deformation and failure are characterized by combined extension and shear (Aimone-Martin et al. 1997). Underground excavations are also subjected to dynamic loads, such as blasting and machinery vibration, which may cause the surrounding rocks to exhibit dynamic deformation and failure behaviour (Zhang and Zhao 2014). Therefore, it is important to study the mechanical behaviour and strength criteria of rocks under compression–shear and tension–shear stress conditions.

The direct shear test is the most common and reasonable method for studying the shear mechanical behaviour of rocks. Direct shear tests have been widely conducted under quasi-static loading to investigate the multi-scale shear behaviour of rocks, such as strength, deformation and fracture mechanisms, for which the normal compressive stress level is usually considered an important influence factor (Petit 1988; Wibberley et al. 2000; Cho et al. 2008; Cai and Liu 2009). The technique of direct shear testing under normal compressive stress is relatively mature, and some standard test methods have been proposed (USACE 1980; ASTM 2008; NSPRC 2013). Conversely, the direct tension–shear test for rocks is difficult to conduct due to the technical constraints of applying a tensile load. Therefore, previous studies have mainly adopted indirect test methods to study the tensile behaviour of rocks, e.g., Brazilian disc and three-point bending tests, to test the tensile strength and fracture toughness (Xeidakis et al. 1997; Al-Shayea 2002; Lin et al. 2009; Aliha et al. 2012; Ren et al. 2016). Brace (1964) first attempted to evaluate the tension–shear strength of rocks through triaxial extension tests using a dog-bone-shaped specimen with a thin centre section and thick ends, which allows the generation of an axial tensile stress when the specimen is subjected to a confining pressure. However, the success rate of producing tension–shear fracture with Brace's method is low (Engelder 1999). Ramsey and Chester (2004) followed the same general methodology as Brace to test Carrara marble but made key modifications to the specimen geometry and jacket design to improve reproducibility. They successfully achieved tension–shear fracture and a continuous transition from tension fracture to shear fracture with increasing confining pressure; moreover, they found that the tension–shear strength is not consistent with a parabolic strength envelope, e.g., the Griffith criterion. Using this improved triaxial extension test method, Rodriguez (2005) further studied the microstructure of the tension-to-shear fracture transition in Carrara marble, and Bobich (2005) applied this test approach to investigate Berea sandstone. Nonetheless, the test method is complicated to perform, e.g., processing of the dog-bone-shaped specimen. In addition Aimone-Martin et al. (1997), designed a symmetrical four-link mechanism for use with an MTS machine to measure the combined tension and shear in a cylindrical rock specimen. However, this mechanism results in tensile deformation being proportional to shear deformation, and the tensile load changes during loading, i.e., the tensile stress and deformation are not isolated from the effects of shear stress and deformation. Recently, Huang and his collaborators designed three auxiliary devices to conduct tension–shear tests of rocks to improve the above deficiencies, containing direct shear (Cen and Huang 2017), double-shear (Huang and Zhu 2018, 2019) and triaxial extension (Zeng et al. 2019).

The loading rate effect on uniaxial/triaxial compression and direct/indirect tension properties of rocks has been investigated extensively using various test methods (Li et al. 1999, 2013, 2014; Cadoni 2010; Dai et al. 2010; Frew et al. 2010; Fuenkajorn and Kenkhunthod 2010; Gong and Zhao 2013; Okubo et al. 2013; Zhang and Zhao 2014). These studies indicated that the loading rate may affect the failure mode, the Young's modulus, the Poisson's ratio, the strain at peak strength, and especially the peak strength, which increases as the loading rate increases (Zhang and Zhao 2014). The loading rate dependency of the most common strength theories, such as the Mohr–Coulomb and Hoek–Brown strength criteria, has also been examined (Zhao 2000; Huang et al. 2012; Xia 2013). Zhao (2000) found that the Mohr–Coulomb criterion is roughly applicable to dynamic strength in the low confining pressure range (as the loading rate increases, the cohesion increases, whereas the internal friction angle seems unaffected), whereas the Hoek–Brown criterion is better to describe the dynamic strength at both low and high confining pressures (the material constant m appears unaffected by the loading rate). Based on a review of previous publications (Crawford and Curran 1981; Barbero et al. 1996; Fukui et al. 2004; Singh et al. 2011; Atapour and Moosavi 2014; Tang and Wong 2016; Wang et al. 2016), the shearing rate effect on shear behaviour is more prevalent in rock joints than in rocks. The dynamic punch shear test has been commonly performed to study the dynamic loading rate effects on rocks (not considering normal compressive stress) (Zhao 2000; Huang et al. 2011, 2012; Xia 2013). However, the reliability of this approach still needs further validation (Zhang and Zhao 2014). Xu et al. (2015) developed a compression–shear loading technique based on the split Hopkinson pressure bar (SHPB) apparatus by adding cushions with oblique surfaces and applied the Drucker–Prager model to describe the strength criterion of granite tested at different loading rates. Fukui et al.

(2004) performed direct shear tests on Sanjome andesite under four constant normal compressive stresses (10, 20, 30, and 40 MPa) and three shearing rates (5×10^{-5}, 5×10^{-4}, and 5×10^{-3} mm/s). They observed that if the shearing rate increased by an order of magnitude, the cohesion increased by approximately 6.1%, whereas the internal friction angle and residual strength did not increase.

The above research status can be summarized as follows. (1) Numerous quasi-static compression–shear tests and few dynamic compression–shear tests of rocks have been carried out; however, both quasi-static and dynamic tension–shear tests are rarely performed. (2) Previous research on the loading rate effect has focused on uniaxial/triaxial compression and direct/indirect tension properties of rocks and shear properties of rock joints. (3) Due to the lack of sufficient tension–shear data, shear strength criteria for rocks have been generally established from compression–shear data and extrapolated into the tension region to represent the tension–shear strength envelope; however, this approach may introduce deviations, e.g., the extrapolated Mohr–Coulomb line may overestimate the actual strength envelope (Goodman 1989).

In this paper, a series of direct shear tests for cuboid sandstone specimens under different constant normal compressive and tensile stresses (namely, compression–shear and tension–shear tests) with different shearing rates were carried out using a servo-controlled compression–shear testing machine. The tension–shear tests were implemented with the help of an auxiliary device that can be used in combination with the compression–shear testing machine. The influences of normal stress and shearing rate on the shear behaviour of the specimens with respect to fracture, deformation, and strength were analysed in detail. A shearing rate-dependent strength criterion for the sandstone specimens was suggested in the full region of the tested normal stress.

2 Test methods

2.1 Specimen preparation

The tested cubic sandstone specimens with a side length of 60 mm were prepared from a sandstone block taken from the Three Gorges Reservoir area of China, as shown in Fig. 1a. The side length of the tested specimens is greater than the minimum value of 50 mm suggested by NSPRC (2013), and the corresponding cross-sectional area of 3600 mm^2 is nearly twice the minimum shear plane area of 1900 mm^2 suggested by ASTM (2008). The tested sandstone is homogeneous without an observable bedding plane. The average bulk density of the sandstone is 2325 kg/m^3. According to the sandstone micrograph shown in Fig. 1b, the grain size ranges from 0.1 to 0.5 mm, and the main minerals are quartz, feldspar, mica, and flint.

2.2 Compression–Shear Testing Machine

In this study, an electrohydraulic servo-controlled compression–shear testing machine was used to perform the direct shear tests with the sandstone specimens under constant normal compression stress conditions, as shown in Fig. 2a. The testing machine contains vertical and horizontal actuators with a loading capacity of 600 kN. The normal stress was applied to the specimen by controlling the vertical actuator, and the shear stress was generated by pushing the lower half of the specimen with the horizontal actuator. The normal and shear deformations of the specimen were measured with two grating displacement sensors with a measurement capacity of 30 mm and an accuracy of 0.001 mm. The setup of the displacement sensors is shown in Fig. 2a. The normal and shear loading rates of the testing machine can be chosen in the range of 0.001–10 mm/min or 0.1–100 kN/min.

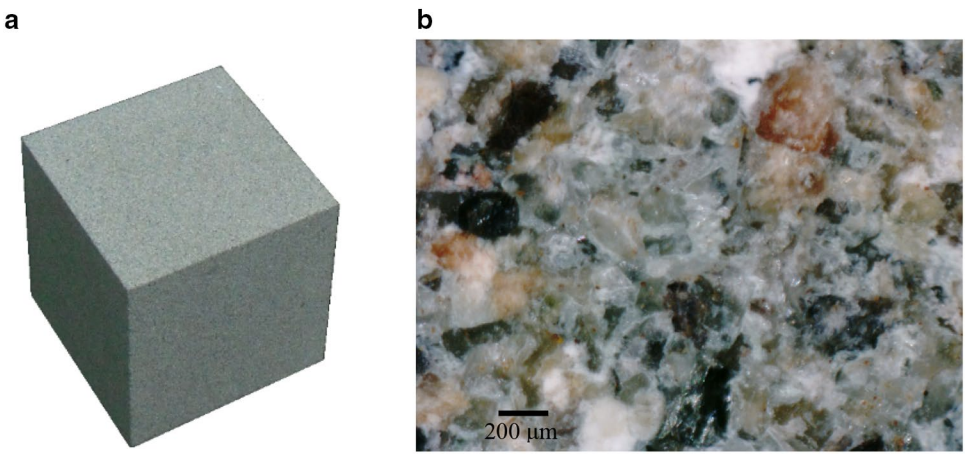

Fig. 1 **a** Photograph of the tested cubic sandstone specimens with a 60 mm side length and **b** a micrograph of the sandstone

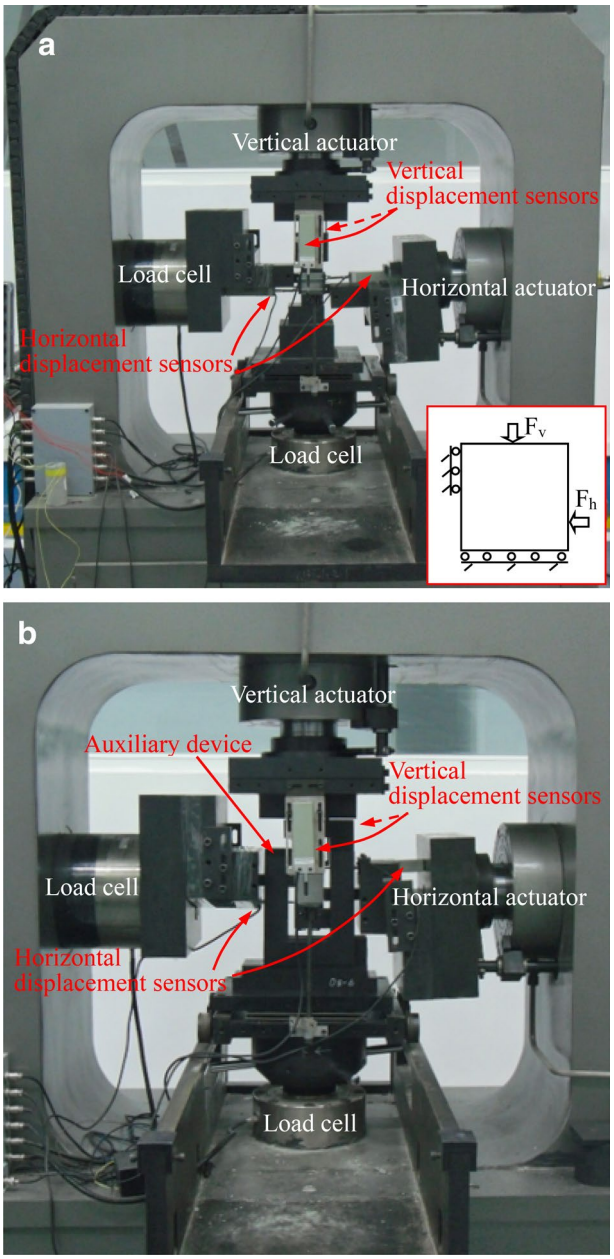

Fig. 2 Electrohydraulic servo-controlled compression–shear testing machine for conducting rock direct shear tests: **a** compression–shear test and **b** tension–shear test (see Fig. 3 for details of the tension–shear auxiliary device)

2.3 An Auxiliary Device for Tension–Shear Testing

A simple auxiliary device for use with the servo-controlled compression–shear testing machine, as shown in Fig. 2b, was proposed in the present study to conduct tension–shear tests. The device, for which the details are shown in Fig. 3, consists of two C-shaped tensioning parts, two L-shaped sliding guide parts, two T-shaped shearing parts, two connecting blocks, and several hexagonal-head bolts. The two tensioning parts can take relative movement along the horizontal and vertical directions independently with the help of the two sliding guide parts by designing sliding tracks (with a trapezoid cross section) in the tensioning parts and matching sliding chutes in sliding guide parts. The device was designed to provide a tension–shear stress state on the plane located in the horizontal centre of the specimen by transforming the compressive load from the vertical actuator of the testing machine to a tensile load on the specimen and applying shear load with the horizontal actuator (Fig. 3a). More details about this device can be seen in the study by Cen and Huang (2017), and the device is described briefly as follows:

Application of normal tensile load The upper and lower surfaces of the cubic specimens were glued to the two connecting blocks using a high-strength structural adhesive with a tensile strength greater than 20 MPa (which can be detached after tests by softening the adhesive via inductive heating), and the two connecting blocks were fastened to the two tensioning parts using hexagonal-head bolts. The specimen was tensioned along the vertical direction when the compressive force was applied to the ends of the two tensioning parts by the vertical actuator of the testing machine.

Application of shear load The horizontal shear load on the specimen was applied when shearing part II was driven by the horizontal actuator of the testing machine. The shear deformation of the lower half of the specimen induced the horizontal movement of tensioning part II along with the sliding guide parts. The frictional resistance of the movement can be minimized by filling a lubricant between the track and the chute.

Measurement of deformation As shown in Fig. 2b, the deformation of the specimen was measured with grating displacement sensors. Normal deformation was obtained by measuring the relative displacement between the vertical actuator and the pedestal below the tension–shear device with two normal displacement sensors. The setup details of the two shear displacement sensors are shown in Fig. 3a.

2.4 Test Procedures

The direct shear behaviour of the sandstone specimens was examined under different constant normal stresses and shearing rates. First, the normal stress was applied to the specimen by controlling the vertical actuator at a loading rate of 0.1 kN/s until the desired level was reached, which was maintained at a constant level in the subsequent shearing process. Then, the horizontal actuator was operated at a constant velocity to apply the shear stress. The compression–shear testing ended when the residual shear

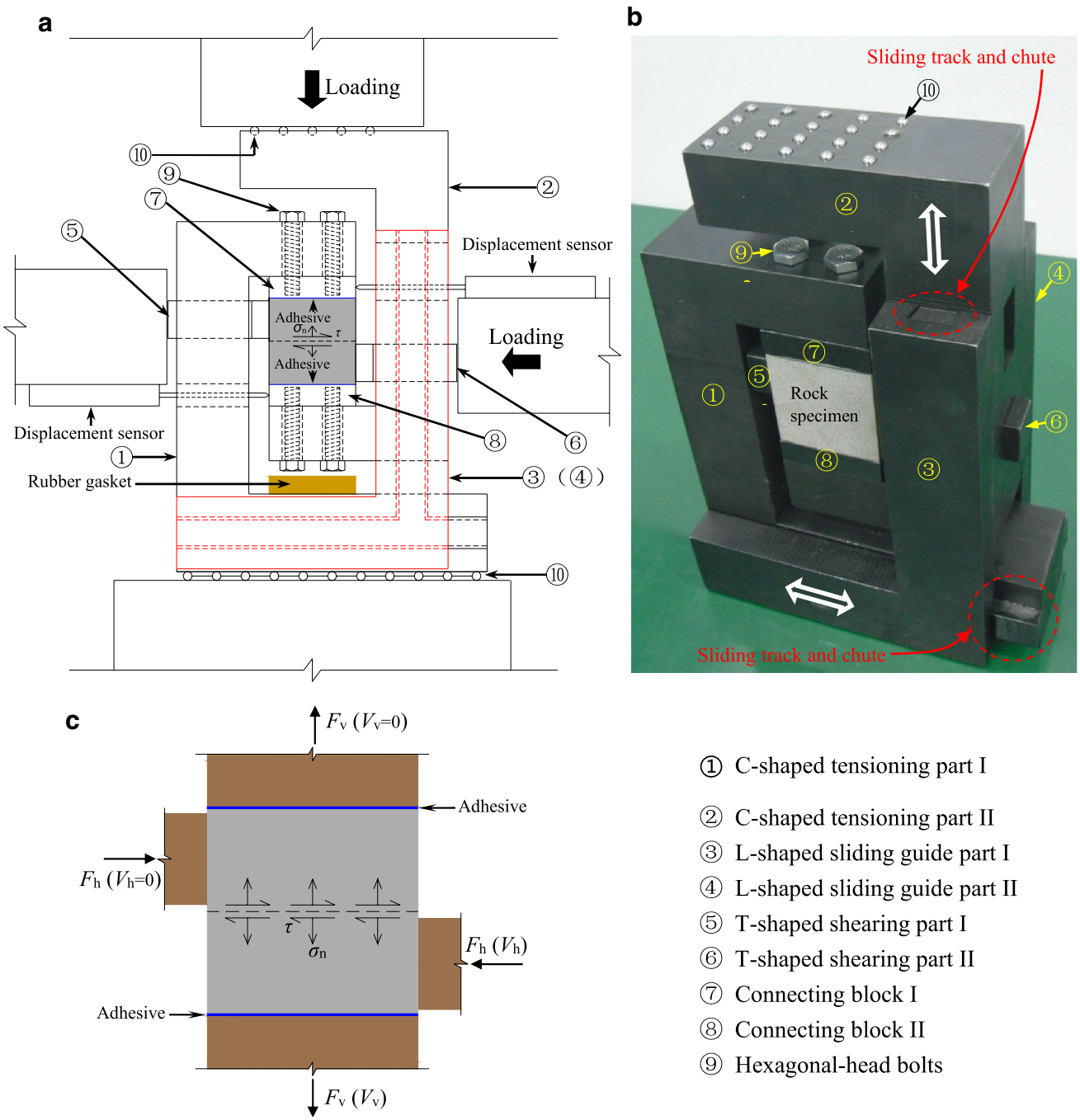

Fig. 3 **a** Schematic of the designed auxiliary device for use with the compression–shear testing machine to conduct tension–shear tests of the cuboid rock specimens, **b** photograph of the manufactured auxiliary device and **c** mechanism of the tension–shear test

stress reached a stable value, and the tension–shear testing ended once the specimen ruptured. At the end of testing, the shear loading was stopped before stopping normal loading for compression–shear testing. Conversely, during the load-controlled tension–shear testing, the normal loading was immediately stopped at the end of testing to ensure safety. Six normal stress levels ($\sigma_n = -3, -2, -1, 1, 3$, and 5 MPa; negative σ_n indicates tensile stress, whereas positive σ_n indicates compressive stress) and four shearing rates ($v = 0.2$, 1, 5, and 10 mm/min) were considered in these tests. A total of 24 conditions were examined. In addition, the uniaxial tension testing for the sandstone was also carried out using the tension–shear device at a vertical loading rate of 0.2 mm/min without applying shear load to obtain the normal stress (namely, tensile strength σ_t) corresponding to shear stress $\tau = 0$.

3 Test Results and Analysis

3.1 Fracture

3.1.1 Fracture Path

Figure 4 shows the typical fracture paths of the tested specimens in the tension–shear and compression–shear tests. The fracture occurs in the predicted shear zone. The figure shows that the aperture of the fracture (after the two upper and lower halves are returned to the original place) becomes wider as the normal stress level increases from tension to compression and that this aperture is much wider for compression–shear cases than for tension–shear cases. The fracture aperture is also wider at a higher shearing rate regardless of tension–shear and compression–shear cases. In addition, stepped fractures with smooth shear risers and rougher extension treads (as shown in Fig. 4g) are found in both tension–shear and compression–shear cases. These features are developed with the coalescence of en echelon cracks (extension cracks) perpendicular to the minimum principal stress direction (Wibberley et al. 2000; Engelder 1999; Rodriguez 2005). The fractures from compression–shear tests are usually accompanied by obvious local spalling that mainly occurs in the shear risers of the stepped fractures, whereas this phenomenon is not apparent in the tension–shear tests. Moreover, the local spalling becomes more obvious as the normal stress level and shearing rate increase in the compression–shear tests. The stepped fracture paths may present different

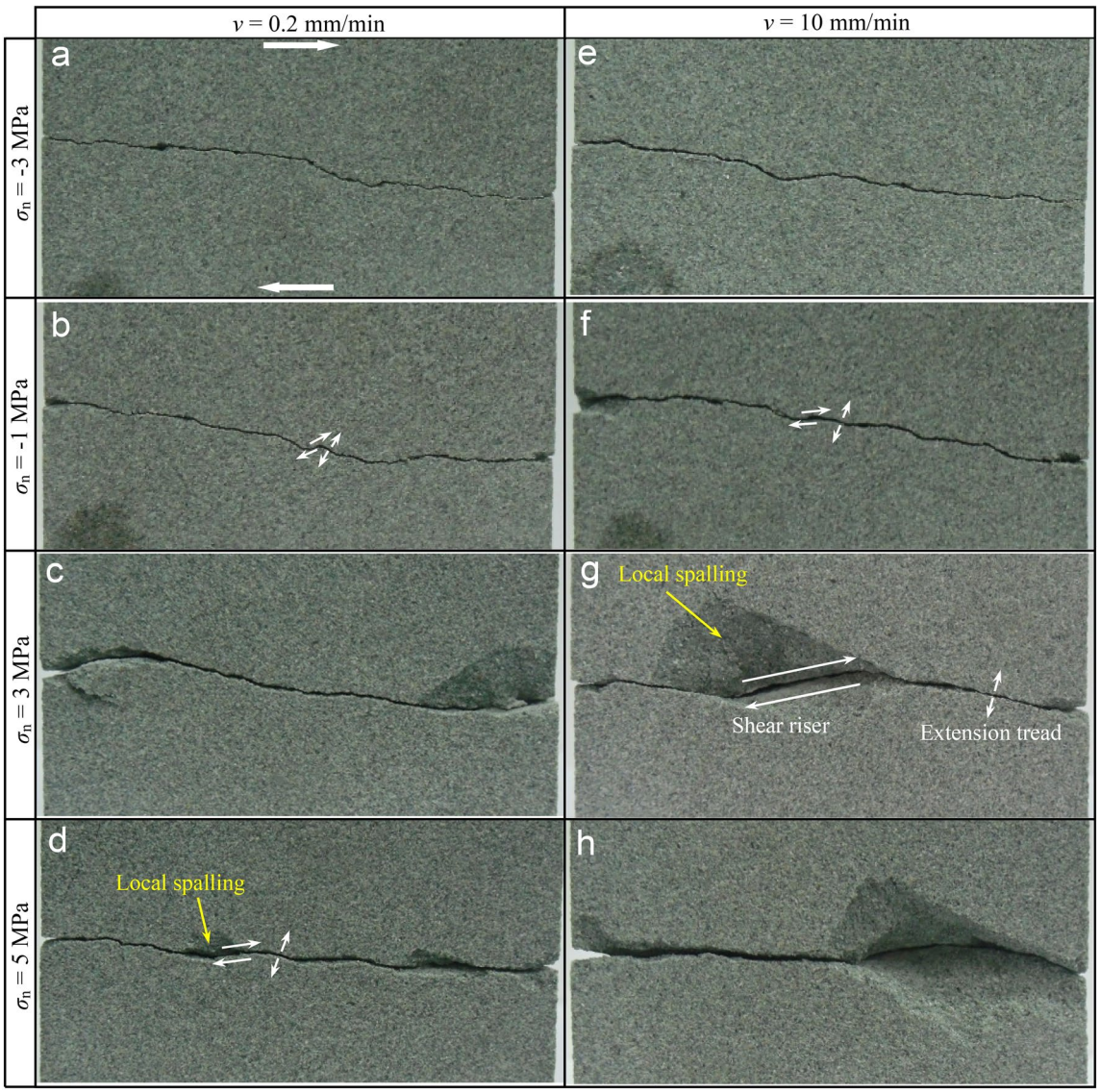

Fig. 4 Typical fracture paths in the tested sandstone specimens

fluctuations under different loading conditions. Taking the compression–shear cases as examples, the fracture path is flatter for a higher normal compressive stress or a lower shearing rate. The above analyses imply that the damage and failure are influenced by both the normal stress level and the shearing rate. The extent of failure in the compression–shear cases is much greater than that in the tension–shear cases due to the higher internal stress and post-peak friction under the compression–shear stress state.

3.1.2 Surface Morphology

Figure 5 shows the typical fracture surface morphologies of the tested specimens. In general, the fracture surface roughness decreases as the stress state changing from tension–shear to compression–shear. Rodriguez (2005) also reported the rough degradation of the fracture surface across the continuous transition from tension fracture to shear fracture in Carrara marble. In addition, fracture surface roughness is greater at a higher shearing rate, as shown in Fig. 5.

For the compression–shear cases, comminution areas (white areas where the grains are comminuted, surrounded by red dotted curves as shown in Fig. 5) and non-comminution areas (except the white areas) can be observed in the fracture surface. The comminution areas are relatively smooth and are accompanied by some slip lineations (as shown in Fig. 5d) along the shear direction due to shearing friction of the upper and lower surfaces of the fracture. Conversely, the non-comminution areas are granular and coarse because there are only intergranular and transgranular fractures without obvious friction marks. For the tension–shear cases, comminution areas are rarely found, which is attributed to the immediate separation of the two sides of the fracture because of the action of the normal tensile force. Therefore, the normal stress direction has an important influence on the fracture surface morphologies of rocks under direct shearing. Note that the fractures in which nearly the full area is covered by comminution areas are usually defined as shear fractures (actually under a relatively high normal compressive stress), whereas the fractures comprising comminution areas and non-comminution areas are defined as hybrid fractures (namely, hybrid tensile and shear fractures) by some researchers (Ramsey and Chester 2004; Rodriguez 2005; Bobich 2005). According to their definitions, a hybrid fracture can occur in the compression–shear test with a low normal compressive stress (Fig. 5c, d, g, h), which shows strong dilation in the process of shearing.

3.2 Shear Stress–Displacement Curves

3.2.1 Compression–Shear Test Curves

Figure 6 displays the shear stress–displacement curves of the tested sandstone obtained from the compression–shear tests under three normal compressive stress levels ($\sigma_n = 1$, 3, and 5 MPa) and four shearing rates ($v = 0.2$, 1, 5, and 10 mm/min). As a typical example, the curve of $\sigma_n = 3$ MPa and $v = 0.2$ mm/min is illustrated in Fig. 7a to emphasize the shear deformation/damage process, which can be divided into five stages: the crack closure stage (OA), the elastic deformation stage (AB), the yield stage (BC), the post-peak failure stage (CD), and the residual friction stage (DE). The pre-peak curve shape (damage process) is analogous to the axial stress–strain curve shape (damage process) of a brittle rock subjected to uniaxial/triaxial compression, as shown in Fig. 7b (Martin and Christiansson 2009). The demarcation points A and B of the shear stress–displacement curve (Fig. 7a) correspond to the crack closure stress σ_{cc}, respectively, and the crack initiation stress σ_{ci} is marked at the axial stress–strain curve (Fig. 7b). Note that the yield stage of the axial stress–strain curve is further divided into two stages (namely, the stable crack growth stage and the unstable crack growth stage) by the crack damage stress σ_{cd}. As illustrated in Fig. 7b, acoustic emission (AE) rates, i.e., damages, start at σ_{ci} and increase drastically when σ_{cd} is reached. Similar damage (crack) development of brittle rock in the direct shear test was simulated by Cho et al. (2008) using the discrete element method (DEM), as shown in Fig. 7c. The shear stress–displacement curve characteristics in each stage are analysed hereafter.

Crack closure stage In this stage, the shear stress–displacement curve is slightly concave-upward resulting from the closure of existing cracks, such as pores and voids, in the rock specimen (Cho et al. 2008), especially the closure occurring in the shear zone due to shearing compaction. The initial nonlinearity of the axial stress–strain curve is also observed in the uniaxial/triaxial compression test (Fig. 7b).

Elastic deformation stage The shear stress–displacement curve increases approximately linearly, i.e., only linear-elastic shear deformation occurs in this stage. Referring to the AE events in the uniaxial/triaxial compression test (Fig. 7b) and crack development in the DEM-simulated direct shear test (Fig. 7c), there is nearly no damage in this stage.

Yield stage This is the crack initiation and propagation stage, presenting a reduction in shear stiffness compared with that in the elastic deformation stage. The shear stress–displacement curve of $\sigma_n = 1$ MPa and $v = 0.2$ mm/min exhibits fluctuations in the yield stage (Fig. 6a), which implies the progressive development of shear rupture. A similar phenomenon can also be observed in the case of $\sigma_n = 5$ MPa and $v = 1$ mm/min (Fig. 6b). The yield stage may also contain earlier stable growth and later unstable growth of cracks, such as the yield stage in the uniaxial/triaxial compression test (Fig. 7b). However, it is difficult to divide these two

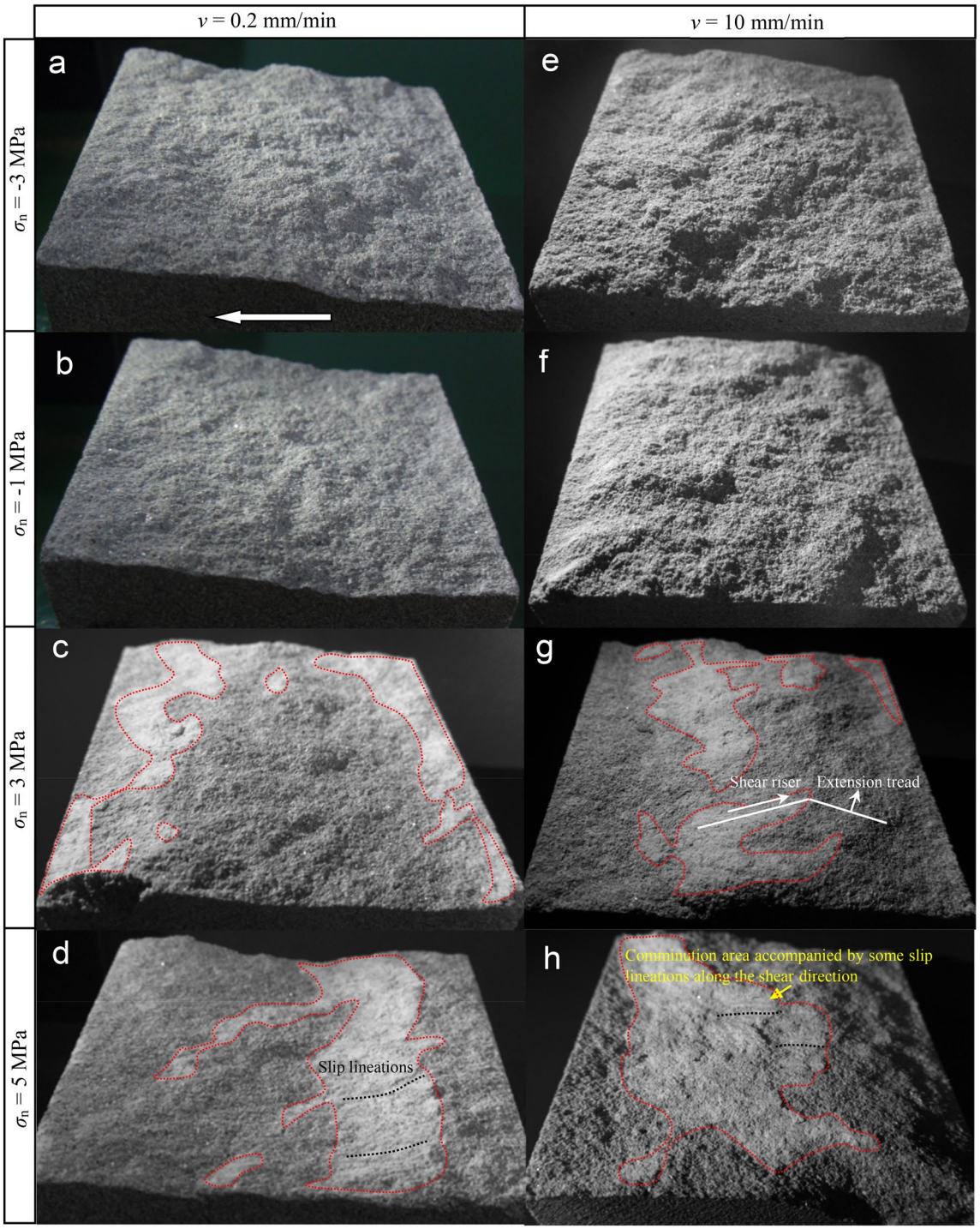

Fig. 5 Typical fracture surface morphologies of the tested sandstone specimens

sub-stages by observing the shear stress–displacement curve in this study, and additional measurement data, such as AE events, are needed to determine this division.

Post-peak failure stage In this stage, the through-going shear fracture forms and the shear stress drop sharply. In the cases of $v = 0.2$ and 1 mm/min (Fig. 6a, b), post-peak plastic deformation can be found before the shear stress sharply drops, whereas this phenomenon does not exist in the cases of $v = 5$ and 10 mm/min (Fig. 6c, d). The post-peak curves in Fig. 6a, b show that the plastic deformation is more obvious (namely, the ductility improves) as the normal compression

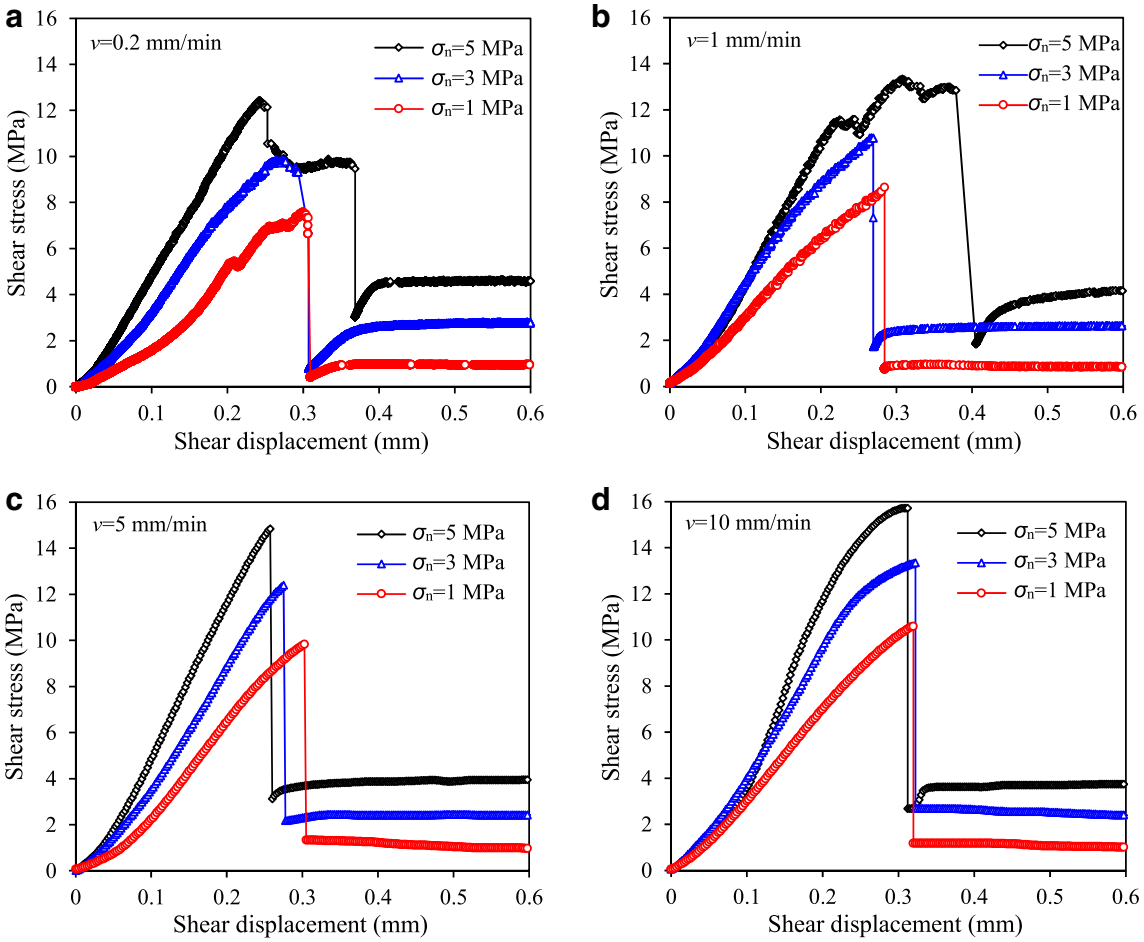

Fig. 6 Shear stress–displacement curves of sandstone obtained from the compression–shear tests

stress level increases. The above results indicate that the sandstone tested under compression–shear generally exhibits significant brittle failure, which becomes stronger with increasing shearing rate but weaker with increasing normal compression stress level.

Residual friction stage Friction between fracture surfaces is the main behaviour in this stage, and the residual shear stress ultimately reaches a stable value. This stage contains the earlier stress recovery. As shown in Fig. 6, the stress recovery becomes slight and even disappears as the shearing rate increases; however, this phenomenon is more obvious as the normal compression stress level increases. The stress recovery phenomenon can also be observed in the shear stress–displacement curves of direct shear tests for synthetic brittle rock ($\sigma_n = 0.81$, 1.23, and 1.64 MPa) carried out by Cho et al. (2008).

Generally, the characteristics of the compression–shear curves are similar to those of the curves from uniaxial/triaxial compression tests, especially the characteristics of the pre-peak curves. These curve characteristics and corresponding failure characteristics are different from those in the tension–shear tests, which are described hereafter.

3.2.2 Tension–Shear Test Curves

Figure 8 displays the shear stress–displacement curves of the sandstone obtained from the tension–shear tests under three normal tensile stress levels ($\sigma_n = -3$, -2, and -1 MPa) and four shearing rates ($v = 0.2$, 1, 5, and 10 mm/min). Figure 9 presents some typical curves to show the difference between tension–shear and compression–shear curves. A comparison of the curves from the tension–shear tests and compression–shear tests suggests that the shear deformation/damage process under normal tensile stress conditions contains the crack closure/opening stage, elastic deformation stage, yield stage, and post-peak failure stage, whereas the residual friction stage is not present due to the separation of the two halves of the specimen when the fracture forms. Unlike the compression–shear cases, the initial nonlinearity of the shear stress–displacement curves for the tension–shear cases is due to both the original crack closure induced by

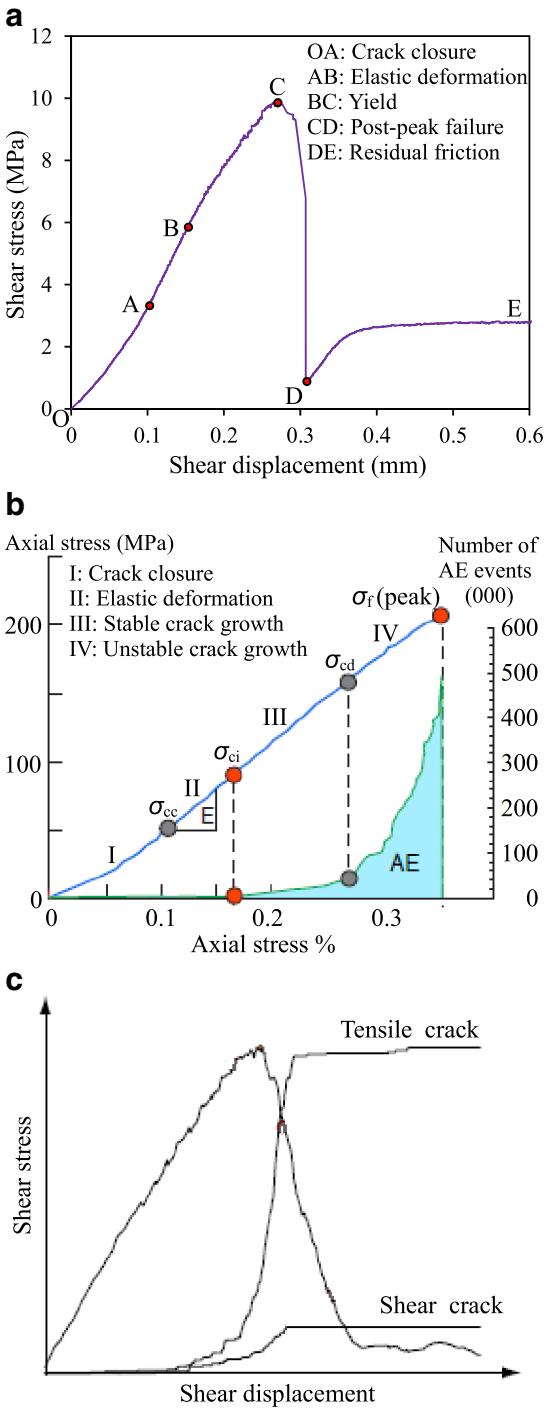

Fig. 7 **a** Typical shear stress–displacement diagram from the compression–shear test showing the stages of sandstone deformation/damage development, **b** typical stress–strain diagram showing the stages of rock deformation/damage development when subjected to uniaxial/triaxial compression (after Martin and Christiansson 2009), and **c** crack development of brittle rock in a direct shear test via DEM simulation (after Cho et al. 2008)

shearing compaction (especially the cracks perpendicular to the shearing direction) and the crack opening induced by normal tension deformation (especially the cracks perpendicular to the tension direction). Other characteristics of the tension–shear test curves that are distinguished from those of the compression–shear test curves are that the stiffness reduction in the yield stage is not obvious (the stiffness is even increased in some cases, e.g., the case of $\sigma_n = -2$ MPa and $v = 5$ mm/min), and there are no observable pre-peak fluctuations or post-peak plastic deformation in all cases. In addition, the shear displacement at the peak stress state in the tension–shear cases is much smaller than that in the compression–shear cases. Moreover, in the tension–shear cases, the shear displacement at the peak stress state increases as the normal stress σ_n increases, whereas that in compression–shear cases slightly decreases. In general, the shape of the curves in the tension–shear cases is similar to that of the curves from conventional uniaxial tension tests. These characteristics imply that the sandstone exhibits more brittle failure in the tension–shear stress state than in the compression–shear stress state.

3.3 Shear stiffness

3.3.1 Shear stiffness in the elastic deformation stage

Shear stiffness represents the resistance of the rock specimen to shear displacement under an applied shear force prior to reaching the peak shear strength. Shear stiffness is calculated by dividing the applied apparent shear stress by the resulting shear displacement, namely, the slope of the shear stress–displacement curve prior to the peak shear strength.

Figure 10a illustrates the variation in the shear stiffness in the elastic deformation stage ($k_{elastic}$) with respect to the normal stress level. As this figure shows, $k_{elastic}$ increases approximately linearly with increasing normal stress levels in both the tension region and the compression region. Moreover, a large increase in $k_{elastic}$ can be observed; taking the condition of $v = 5$ mm/min as an example, $k_{elastic}$ increases 119.22% and 62.39% as σ_n increases from -3 to -1 MPa and 1 to 5 MPa, respectively. In general, the stress-dependent increase rate of $k_{elastic}$ (namely, the slope of $k_{elastic}$ versus σ_n) increases as the shearing rate increases, which implies that the sensitivity of $k_{elastic}$ to the normal stress level is influenced by the shearing rate. In addition, the increase rate of $k_{elastic}$ in the tension region is close to that in the compression region as a whole. Thus, the normal stress direction has no obvious influence on the sensitivity of $k_{elastic}$ to normal stress levels.

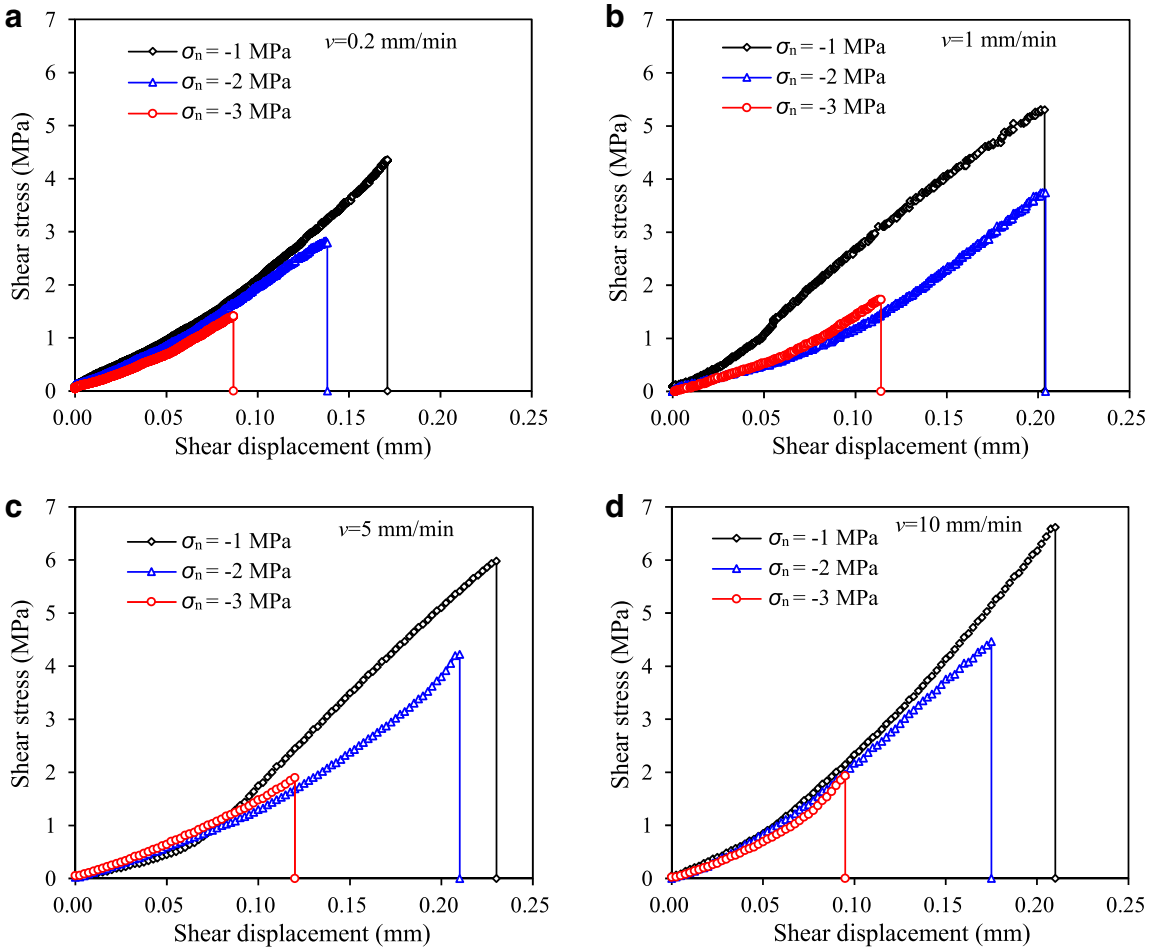

Fig. 8 Shear stress–displacement curves of sandstone obtained from the tension–shear tests

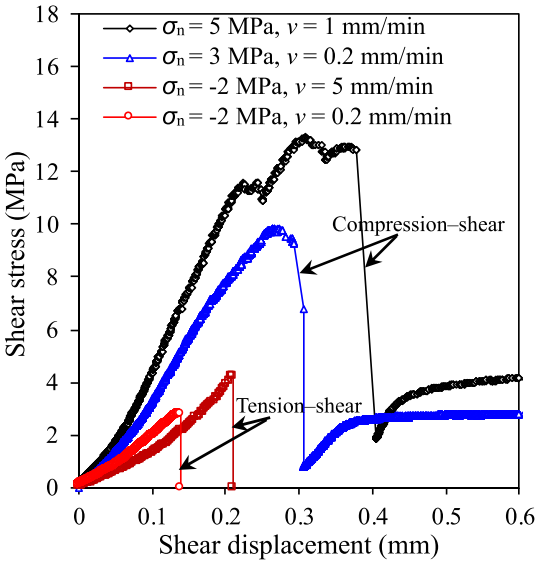

Fig. 9 Difference between tension–shear and compression–shear curves of sandstone

Figure 10b illustrates the variation in $k_{elastic}$ with respect to the shearing rate. Generally, $k_{elastic}$ slightly increases with increasing shearing rate, thereby presenting an approximately linear relationship; however, some data are discrete in some cases. The speed-dependent increase rate of $k_{elastic}$ is greater when the normal stress level is higher, which indicates that the sensitivity of $k_{elastic}$ to shearing rate is influenced by the normal stress level.

3.3.2 Pre-peak average shear stiffness

The pre-peak average shear stiffness ($k_{average}$), which is defined as the ratio of the peak shear strength to the peak shear displacement, represents the overall resistance of rock to shear deformation before failure. Figure 11a shows the variation in $k_{average}$ with respect to the normal stress level. Similar to $k_{elastic}$, $k_{average}$ increases approximately linearly with increasing normal stress level in both the tension region and the compression region. Furthermore, the variations

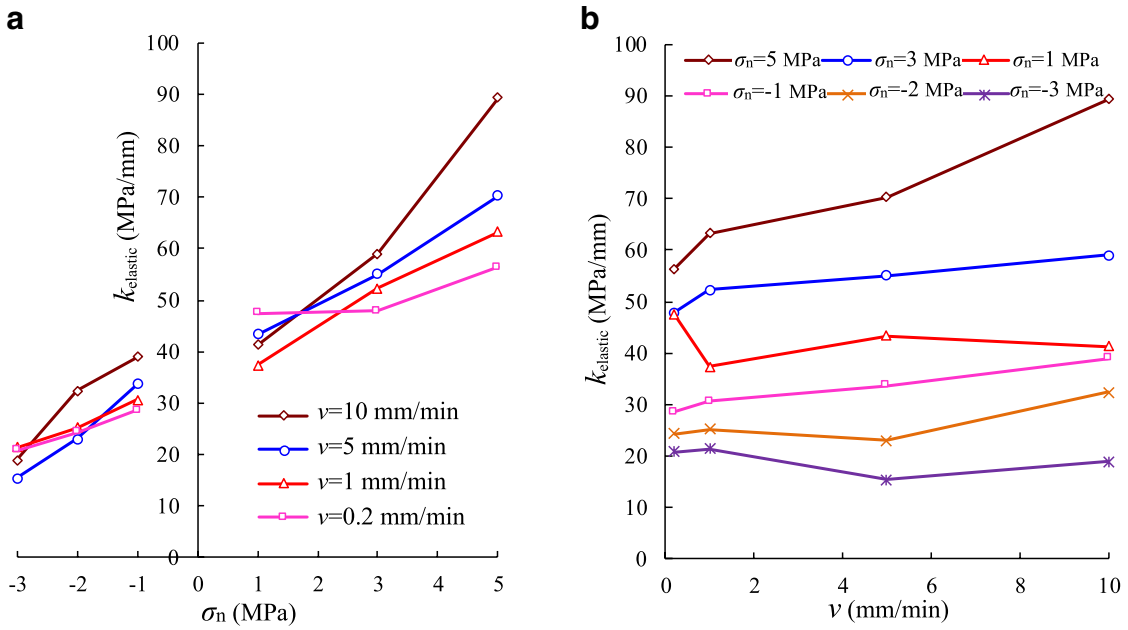

Fig. 10 Variations in the shear stiffness in the elastic deformation stage $k_{elastic}$ with respect to the **a** normal stress level σ_n and **b** shearing rate v

in the average $k_{average}$ and $k_{elastic}$ with respect to the normal stress in the full region (from tension to compression) are presented in Fig. 11b, which are both linear in general ($k_{average}$ is slightly discrete at the tension–compression translation region, which may be due to the discreteness of the sample mechanical properties). However, the increase rate of average $k_{average}$ (4.04 mm^{-1}) is smaller than that of average $k_{elastic}$ (6.05 mm^{-1}). In addition, unlike $k_{elastic}$, the influence of shearing rate on the stress-dependent increase rate of $k_{average}$ (namely, the slope of $k_{average}$ versus σ_n) is small in general.

Figure 11c shows the variation in $k_{average}$ with respect to the shearing rate. Generally, $k_{average}$ changes in a nonlinear manner with increasing shearing rate, which is distinguished from $k_{elastic}$. An interesting finding is observed that the curve connecting the data points is concave-upward (i.e., $k_{average}$ decreases first and then increases with increasing shearing rate) when the normal stress is in tension, whereas the curve is concave-downward when the normal stress is in compression (i.e., $k_{average}$ increases first and then decreases with increasing shearing rate). The concavity becomes more prominent at a higher normal stress level. The average variation tendencies of $k_{average}$ for normal tensile and compressive stress conditions are also presented separately in Fig. 11c. The variation tendencies imply that $k_{average}$ reaches a minimum at $v = 1$ mm/min for the tensile normal stress and reaches a maximum at $v = 5$ mm/min for the compressive normal stress.

Note that some test data deviate from the overall trend due to the discreteness of the sample mechanical properties, as shown in Figs. 10 and 11. For example, the shear stress–displacement curve for the case of $\sigma_n = 1$ MPa and $v = 0.2$ mm/min exhibits a steep elastic deformation section, resulting in an overly large $k_{elastic}$, as shown in Fig. 10, and the shear stress–displacement curve for the case of $\sigma_n = 5$ MPa and $v = 1$ mm/min exhibits a large fluctuation in the pre-peak yield section, resulting in an excessively small $k_{average}$, as shown in Fig. 11.

3.4 Shear Strength

3.4.1 Peak Shear Strength

Some researchers (Nicksiar and Martin 2013; Hoek and Martin 2014; Patel and Martin 2018) have studied the envelope characteristics of rock strength in the region where the minor principal stress transitions from tension to compression under the triaxial stress state. This paper examines the envelope characteristics of direct shear strength and the shearing rate effect in the transition region of normal stress from tension to compression. Figure 12a shows the peak shear strength τ of the sandstone specimens obtained from the compression–shear and tension–shear tests. The uniaxial tensile strength σ_t, namely, the normal stress level σ_n corresponding to shear stress $\tau = 0$, is also presented in Fig. 12a. Therefore, the full region of σ_n ranging from -3.5 to 5 MPa is considered here. The trend lines of the peak shear strength variation with respect to the normal stress level under different shearing rates meet at the point of uniaxial tensile strength. The peak shear strength is more sensitive to the

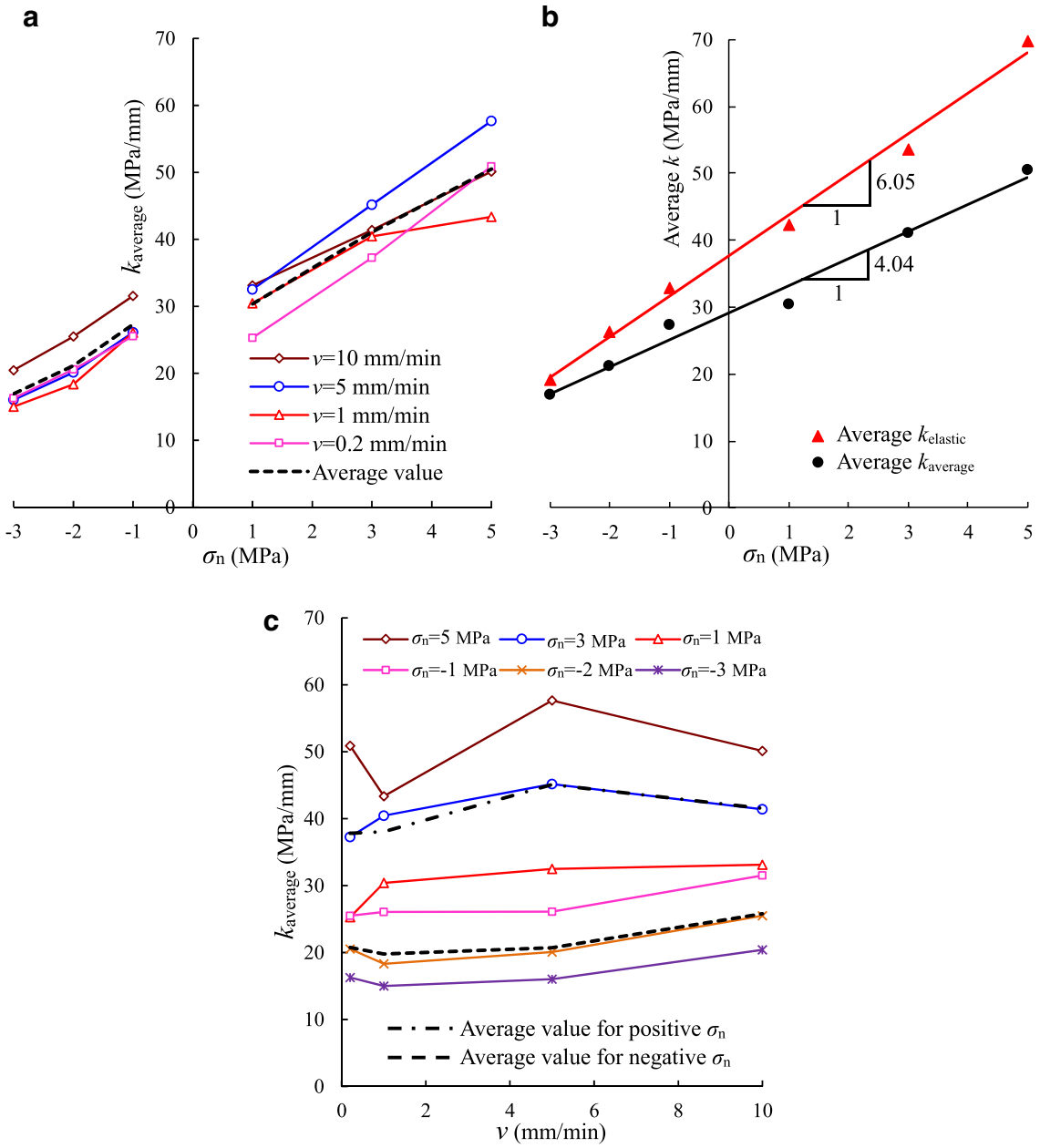

Fig. 11 **a** Variations in the pre-peak average shear stiffness $k_{average}$ with respect to the normal stress level σ_n, **b** variations in the average $k_{elastic}$ and $k_{average}$ with respect to σ_n, and (c) variations in the $k_{average}$ with respect to the shearing rate v

normal tensile stress than to the normal compressive stress, as demonstrated by the steeper slope of the shear stress versus normal stress curve in the tension region, particularly when approaching the uniaxial tensile strength. The sensitivity of the peak shear strength to the normal tensile stress is enhanced when the shearing rate is increased. The peak shear strength in the tension region shows a nonlinear variation, whereas that in the compression region varies approximately linearly. To obtain the peak shear strength parameters in the compression region, the linear Mohr–Coulomb strength envelopes (solid lines; the root-mean-square errors (RMSEs) for four shearing rates of 0.2, 1, 5 and 10 mm/min are 0.064, 0.099, 0.040 and 0.106 MPa, respectively) are drawn in Fig. 12a. The variations in the cohesion (c) and the internal friction angle (φ) with respect to the shearing rate are also shown in Fig. 12a. The cohesion increases obviously in a nonlinear manner with increasing shearing rate, and this increase rate is observed to decrease with increasing shearing rate. As the shearing rate increases from 0.2 to 10 mm/min, the cohesion increases by 48.40%. However, the internal friction angle seems unaffected by the shearing rate: it only increases by approximately 1.7° as the shearing

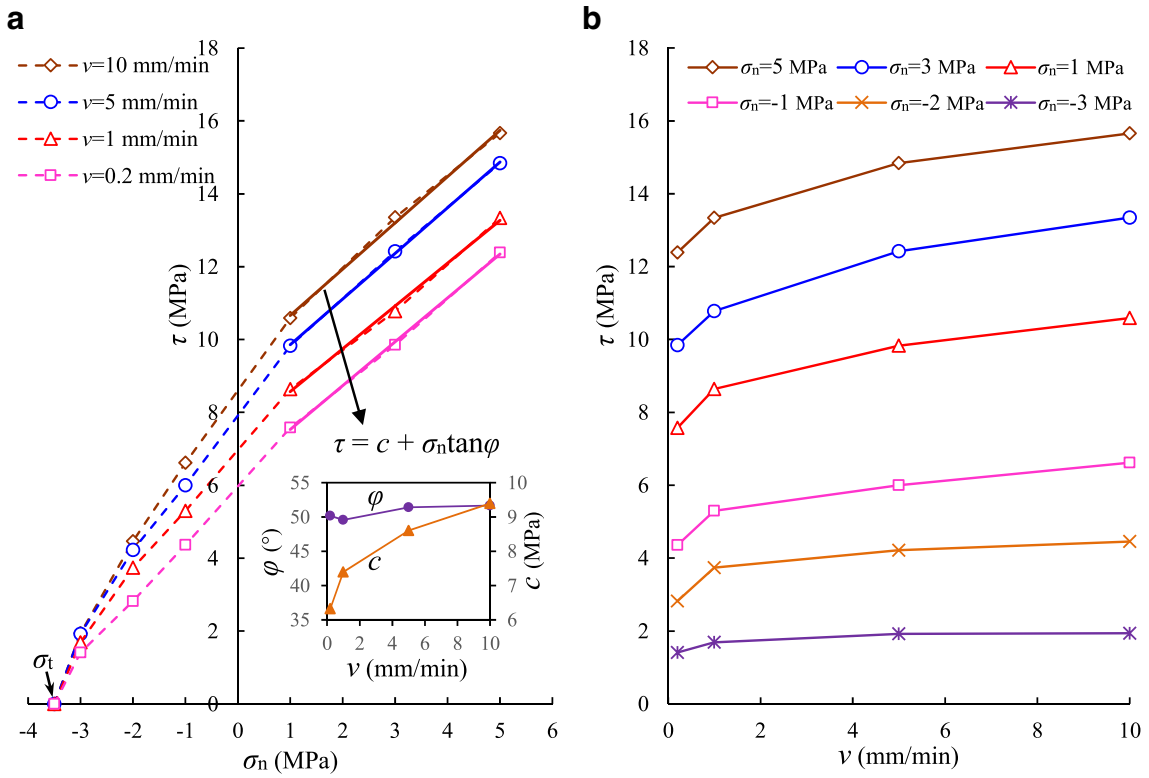

Fig. 12 Variations in the peak shear strength τ with respect to the **a** normal stress level σ_n and **b** shearing rate v

rate increases from 0.2 to 10 mm/min. The direct shear tests on Sanjome andesite and the triaxial compression tests on Bukit Timah granite from Singapore carried out by Fukui et al. (2004) and Zhao (2000) presented similar results, in which cohesion increased and the internal friction angle was unaffected with increasing loading rate.

Figure 12b illustrates the variation in the peak shear strength with respect to the shearing rate. The peak shear strength nonlinearly increases as the shearing rate increases, and this increase rate is observed to decrease with increasing shearing rate. The increase rate is nearly unaffected by the level of normal compressive stress, whereas the increase rate slightly increases as the level of normal tensile stress increases. This implies that normal tensile stress affects the sensitivity of the peak shear strength to the shearing rate, whereas normal compressive stress does not.

3.4.2 Residual Shear Strength for Compression–Shear Cases

The residual shear strength τ for the tension–shear case cannot be obtained due to the separation of the two halves of the specimen after fracture formation (this parameter can perhaps be determined via a compression–shear test after the two upper and lower halves are returned to the original place, but the residual shear strength would be measured under normal compressive stress and not under normal tensile stress). Therefore, only the residual shear strength values for the compression–shear cases are analysed herein. As shown in Fig. 13a, the linear Mohr–Coulomb criterion can provide a good fitting for the residual shear strength at each shearing rate. The friction angle decreases and converges gradually as the shearing rate increases. The variation in the residual shear strength with respect to the shearing rate is plotted in Fig. 13b. The residual shear strength decreases nonlinearly with increasing shearing rate (relatively fast at first and then slow later). The effect becomes weaker as the shearing rate increases and more prominent at a higher normal stress level. This finding indicates that normal compressive stress affects the sensitivity of the residual shear strength to the shearing rate.

4 Shearing Rate-Dependent Strength Criterion

4.1 Form of the Strength Envelope

To determine a satisfying strength envelope in the full region of normal stress of the sandstone tested under different shearing rates, the following typical strength criteria were examined:

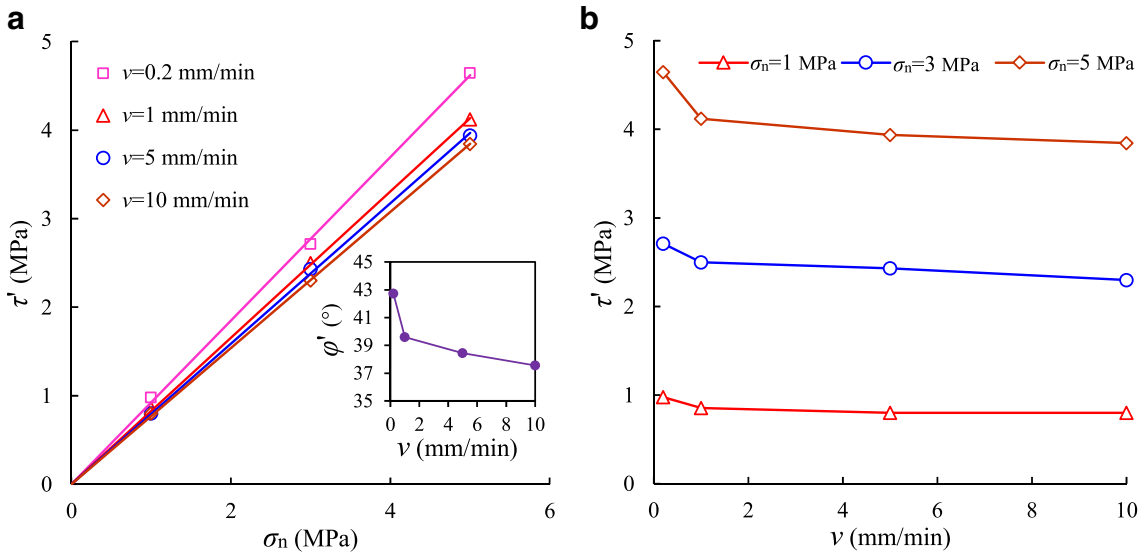

Fig. 13 Variations in the residual shear strength τ with respect to the **a** normal stress level σ_n and **b** shearing rate v

1. *Mohr–Coulomb criterion* The linear Mohr–Coulomb criterion is widely applied in geotechnical engineering. This criterion has a good fitting effect in the compression region of normal stress, as analysed in Sect. 3.4.1 (the RMSE is only 0.040–0.106 MPa). However, the fitting effect becomes worse when the criterion is applied to the full region of normal stress, as shown in Fig. 14a (the RMSE is 1.158—2.481 MPa). Therefore, a nonlinear strength criterion should be considered.
2. 2. *Griffith criterion* The Mohr envelope of the Griffith criterion for biaxial stresses (Paterson and Wong 2005) is expressed as

$$\tau^2 - 4\sigma_n\sigma_t = 4\sigma_t^2 \tag{1}$$

This expression is a parabola containing only one parameter σ_t. Therefore, the prediction curves are the same for different shearing rates, which is not appropriate for predicting the strength of the tested sandstone, as shown in Fig. 14a.

3. *Modified Griffith criterion* The Mohr envelope of the modified Griffith criterion in biaxial stress state (Paterson and Wong 2005) is expressed as

$$\tau = 2\sigma_t\sqrt{1+\frac{\sigma_c'}{\sigma_t}} + \mu\left(\sigma_n - \sigma_c'\right) \tag{2}$$

where μ is the coefficient of friction on the crack faces and σ_c' is the critical macroscopic compressive stress perpendicular to the crack that is needed to close the crack. Note that this criterion has the same form as the Mohr–Coulomb criterion, in which the "cohesion" c is equal to $2\sigma_t\sqrt{1+\sigma_c'/\sigma_t} - \mu\sigma_c'$ and the "coefficient of internal friction" $\tan\varphi$ is equal to μ. Therefore, the fitting effect of the modified Griffith criterion is equivalent to that of the Mohr–Coulomb criterion.

4. *Hoek–Brown criterion* The Hoek–Brown criterion is a widely used strength criterion for rocks. The Mohr envelope of the Hoek–Brown criterion (Hoek and Brown 1980) is expressed as

$$\tau = A\left(\sigma_n - \sigma_t\right)^B \tag{3}$$

in which σ_t for intact rocks is given by

$$\sigma_t = \frac{1}{2}\sigma_c\left(m - \sqrt{m^2+4}\right) \tag{4}$$

where A and B are constants depending upon the material constant m and σ_c is the uniaxial compressive strength. In this study, σ_t is directly determined as the tested uniaxial tensile strength (− 3.5 MPa), whereas A and B are determined by least squares fitting based on the tested data. The fitting results are shown in Fig. 14b. The Hoek–Brown criterion has the best fitting effect (the RMSE is only 0.133–0.234 MPa) among these four strength criteria. Therefore, it was determined to be the optimal criterion to represent the shear strength envelope in the full region of normal stress for the tested sandstone under different shearing rates.

To examine the relationship between A (B) and m for different shearing rates, m for each shearing rate was calculated using Eq. (4). In this equation, σ_c was determined as the value of σ_n at the crossing point of the σ_n axis and the

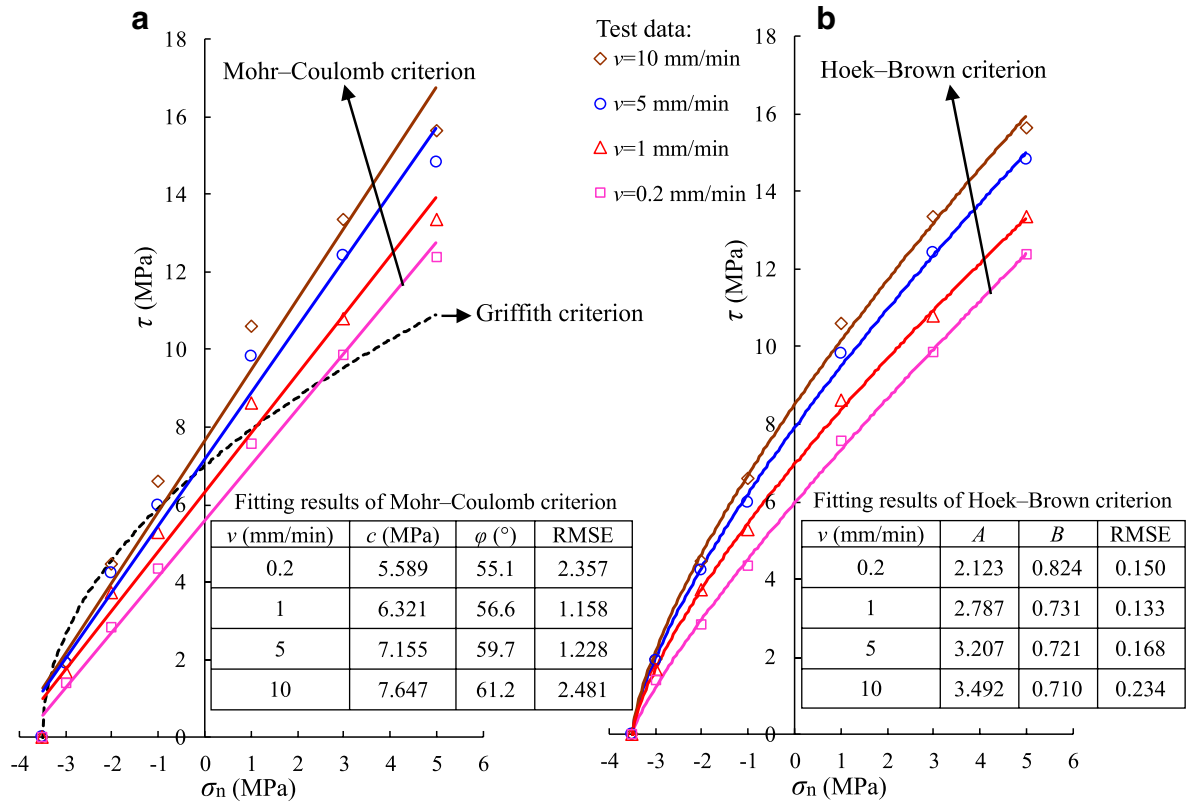

Fig. 14 Examination of different strength criteria for the tested sandstone at different shearing rates: **a** Mohr–Coulomb criterion and Griffith criterion and **b** Hoek–Brown criterion

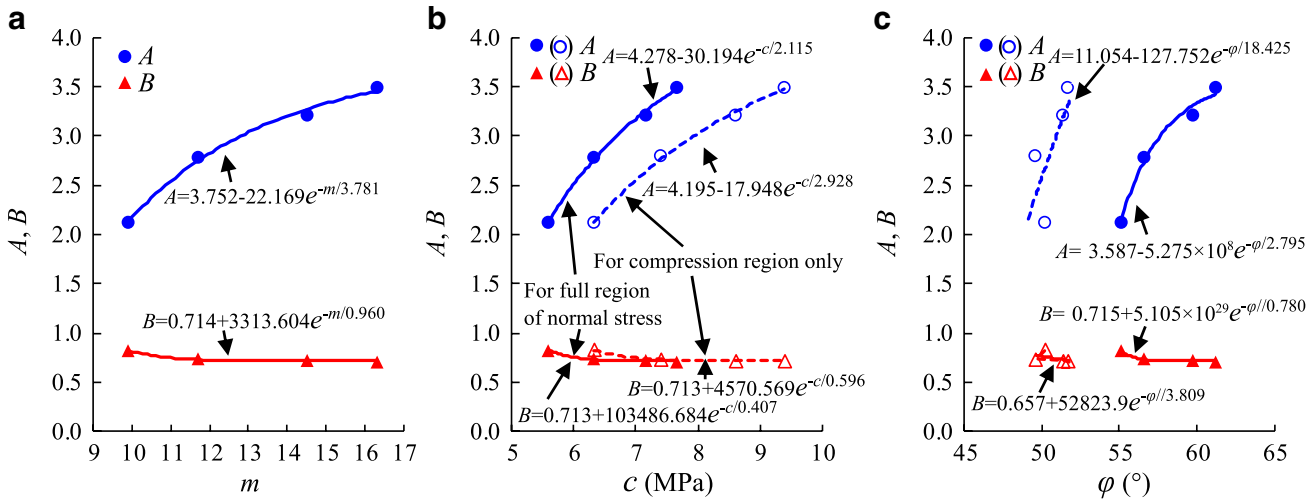

Fig. 15 Mathematical relationships between parameter A (B) and **a** m, **b** c and **c** φ

Mohr's stress circle, which passes through the origin and is tangent to the Hoek–Brown envelope in the compression region of normal stress. The determined σ_c for four shearing rates of 0.2, 1, 5 and 10 mm/min are 34.436, 41.212, 50.954 and 57.359 MPa, respectively, and the corresponding calculated m values are 9.9, 11.7, 14.5 and 16.3, respectively. Figure 15a shows the relationship between A (B) and m, i.e., A increases and B decreases nonlinearly with increasing m, which can be represented as

$$A \quad \text{or} \quad B = a + be^{-m/t} \tag{5}$$

where a, b and t are fitting parameters, as shown in Fig. 15a.

In addition, the relationship between A (B) and c (φ) of the Mohr–Coulomb criterion applied in the full region and only in the compression region of normal stress were examined. The results are similar to those for m and can also be represented using Eq. (5), as shown in Fig. 15b, c.

4.2 Incorporation of the Shearing Rate Effect

Figure 16a illustrates the variations in parameters A and B with respect to the shearing rate v. Parameter A increases and parameter B decreases nonlinearly with increasing shearing rate. The natural logarithm function can represent the mathematical relationship between parameter A (B) and the shearing rate. The fitting results are expressed as

$$A = 0.339 \ln v + 2.7074 \tag{6}$$

$$B = -0.027 \ln v + 0.7622 \tag{7}$$

Thus, parameters A and B are linearly dependent, and their relationship is expressed as

$$B = -0.0796A + 0.9778 \tag{8}$$

After substituting Eqs. (6) and (7) into Eq. (3), a shearing rate-dependent Hoek–Brown strength criterion for the tested sandstone in the full region of the tested normal stress can be expressed as

$$\tau = (0.339 \ln v + 2.7074)\left(\sigma_n - \sigma_t\right)^{(-0.027 \ln v + 0.7622)} \tag{9}$$

Figure 16b displays the predicted strength envelopes for different shearing rates using Eq. (9), i.e., using the mathematical relationships of Eqs. (6) and (7) in the Hoek–Brown criterion. The RMSEs between the predicted and tested data for the four shearing rates of 0.2, 1, 5 and 10 mm/min are 0.195, 0.277, 0.192 and 0.294 MPa, respectively.

Figure 17 shows the influences of parameters A and B on the shape of the strength envelope. Parameter A affects the slope of the strength envelope in the full region of normal stress, whereas parameter B mainly affects that in the region of normal stress > -2.5 MPa. These findings mean the shearing rate effect in the region of normal stress < -2.5 MPa is adjusted mainly by parameter A, whereas that in the region of normal stress > -2.5 MPa is adjusted jointly by parameters A and B. Since the variations in parameters A and B with respect to the shearing rate are inverse (Fig. 16a), it is possible to control the influence of the shearing rate on the slope of the strength envelope in a small range in the compression region of normal stress, presenting a slight change in the internal friction angle with respect to the shearing rate, as analysed in Sect. 3.4.1.

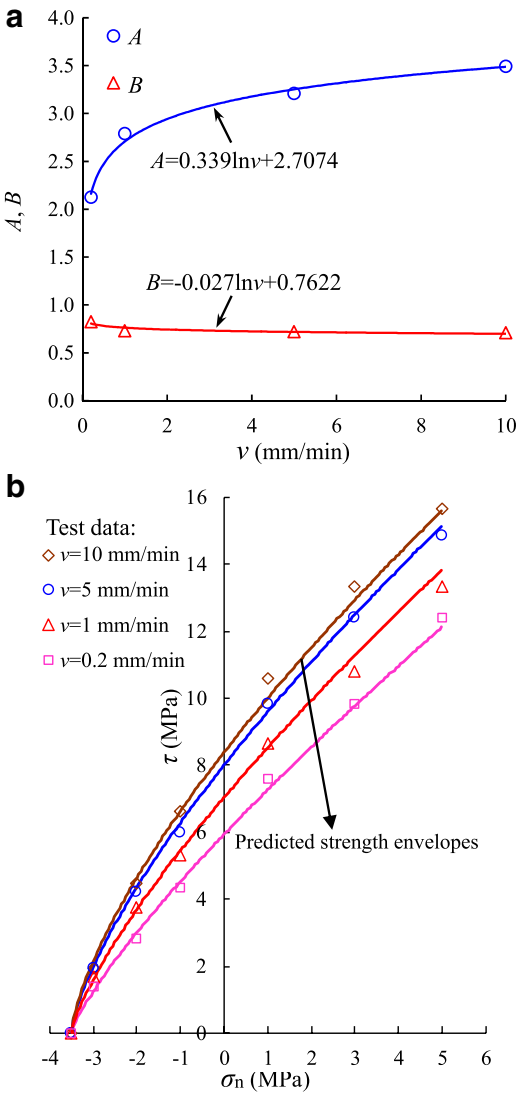

Fig. 16 **a** Mathematical relationship between parameter A (B) and the shearing rate v and **b** the predicted strength envelopes using these relationships in the Hoek–Brown criterion

5 Conclusions and Discussion

The compression–shear and tension–shear behaviour, including fracture, deformation, and strength, of cuboid sandstone specimens were experimentally investigated under different normal stress ($\sigma_n = -3$, -2, and -1 MPa for tension and 1, 3, and 5 MPa for compression) and shearing rate ($v = 0.2$, 1, 5, and 10 mm/min) conditions. A simple mechanical device was designed and constructed to conduct the tension–shear tests, which can also be used in a servo-controlled compression–shear testing machine. The main conclusions of this

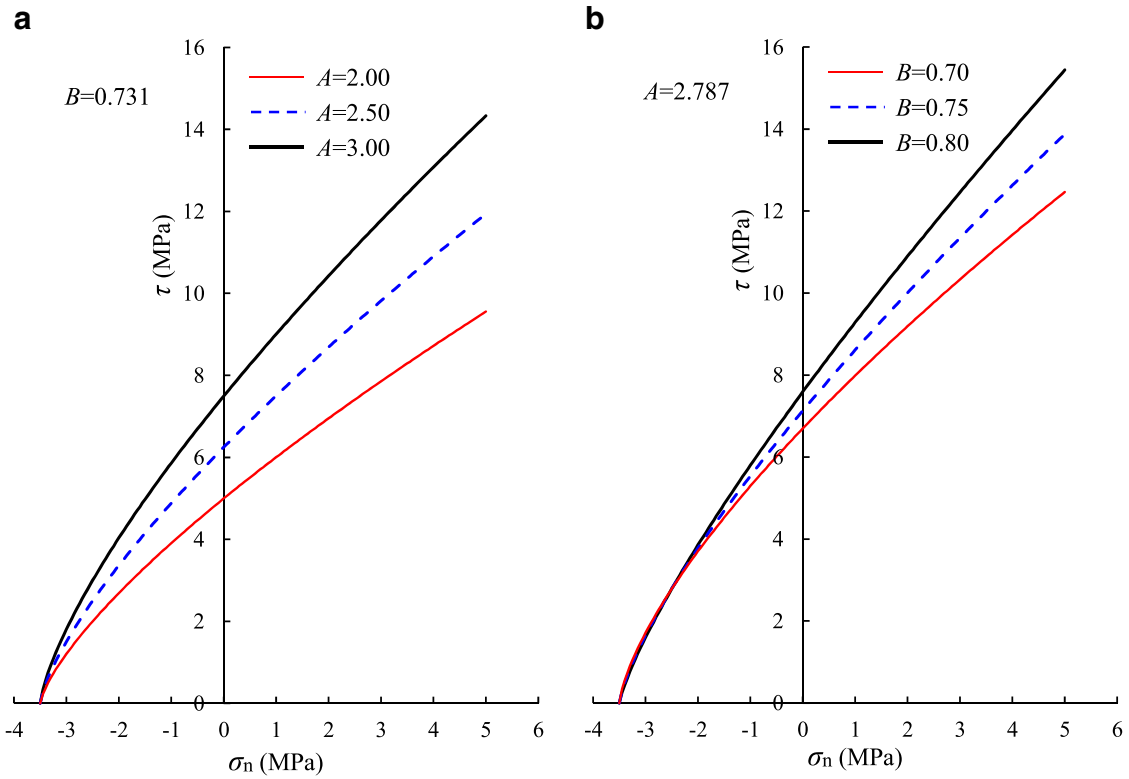

Fig. 17 Influences of parameters **a** A and **b** B on the shape of the strength envelope

study, especially the difference between compression–shear and tension–shear cases, are summarized as follows:

1. The damage of the fracture, such as the aperture of fractures and the local spalling observed in the lateral views of the fractures, becomes more obvious as the normal stress level and shearing rate increase for both tension–shear and compression–shear tests. Generally, the fracture surface roughness decreases as the stress state changes from tension–shear to compression–shear and increases with increasing shearing rate. The grain comminution in the fracture surface is obvious in the compression–shear cases, whereas this phenomenon is slight in the tension–shear cases. In general, the extent of failure in the compression–shear cases is much greater than that in the tension–shear cases.
2. Stiffness reduction in the yield stage and plastic deformation in the post-peak failure stage (for some cases) are observed in the shear stress–displacement curves for the compression–shear cases. However, for the tension–shear cases, the stiffness reduction is not obvious, and there is no observable post-peak plastic deformation. These results imply that the sandstone presents more brittle failure in the tension–shear stress state than in the compression–shear stress state. In addition, the brittle failure becomes weaker with increasing normal stress level and stronger with increasing shearing rate for the compression–shear cases.
3. The shear stiffness in the elastic deformation stage (k_{elastic}) increases approximately linearly with increasing normal stress level for both tension–shear and compression–shear cases. Generally, k_{elastic} increases with increasing shearing rate, which also presents an approximately linear relationship. The variation in the pre-peak average shear stiffness (k_{average}) with respect to the normal stress level is similar to that in k_{elastic}. Unlike k_{elastic}, k_{average} increases first and then decreases with increasing shearing rate for tension–shear cases; however, k_{average} decreases first and then increases with increasing shearing rate for compression–shear cases.
4. The peak shear strength is more sensitive to normal tensile stress than to normal compressive stress, showing a nonlinear variation in the tension region and an approximately linear variation in the compression region. The peak shear strength nonlinearly increases as the shearing rate increases, and this increase rate decreases with increasing shearing rate. The variation in the residual shear strength is similar to that in the peak shear strength with respect to the normal stress and inverse to that with respect to the shearing rate. The linear Mohr–Coulomb strength envelopes in the compression region of normal stress indicate that the cohesion increases and converges

gradually, whereas the internal friction angle seems unaffected with increasing shearing rate.

5. The Hoek–Brown criterion involving the shearing rate effect ($\tau = A(\sigma_n - \sigma_t)^B$, where $A = 0.339 \ln v + 2.7074$ and $B = -0.027 \ln v + 0.7622$) was deemed the optimal shearing rate-dependent nonlinear strength criterion for the tested sandstone in the full region of tested normal stress. The relationship between the fitting parameter A (B) and the material constant m of the Hoek–Brown criterion for different shearing rates and the relationship between the fitting parameter A (B) and the shear strength parameter c (φ) of the Mohr–Coulomb criterion were revealed. The influences of parameters A and B on the shape of the Hoek–Brown strength envelope were examined.

This study is more in-depth and comprehensive than our previous studies (Cen and Huang 2017; Huang and Zhu 2018, 2019), which were mainly aimed at the tension–shear behaviour of sandstone and considered only one shearing rate. The differences in fracture, shear stress–displacement curve shape and shear stiffness between the compression–shear and tension–shear cases in this study are similar to those in our previous studies; nevertheless, more detailed investigations were carried out in this study, and more abundant results were presented as described above. Both this study and our previous studies indicate that the shear strength of the tested sandstone varies approximately linearly in the compression–shear stress state and nonlinearly in the tension–shear stress state, which can be described by the Hoek–Brown criterion. Furthermore, a shearing rate-dependent Hoek–Brown strength criterion was proposed in this study. However, only sandstone was tested in our studies, and other kinds of rocks need to be tested to examine the applicability of the Hoek–Brown criterion.

Acknowledgements This work is supported by the National Natural Science Foundation of China (Nos. 41807279, 41672300 and 41972297), the Natural Science Foundation of Hebei Province, China (No. E2019202336) and the Supporting program of hundred promising innovative talents in Hebei provincial education office (No. SLRC2019027).

References

Aimone-Martin CT, Oravecz KI, Nytra TK (1997) A mechanical device for the measurement of combined shear and tension in rocks. Int J Rock Mech Min Sci 34(1):147–151. https://doi.org/10.1016/S1365-1609(97)80041-X

Aliha MRM, Ayatollahi MR, Akbardoost J (2012) Typical upper bound–lower bound mixed mode fracture resistance envelopes for rock material. Rock Mech Rock Eng 45(1):65–74. https://doi.org/10.1007/s00603-011-0167-0

Al-Shayea N (2002) Comparing reservoir and outcrop specimens for mixed mode I–II fracture toughness of a limestone rock formation at various conditions. Rock Mech Rock Eng 35(4):271–297. https://doi.org/10.1007/s00603-002-0027-z

ASTM D5607–08 (2008) Standard test method for performing laboratory direct shear strength tests of rock specimens under constant normal force. ASTM International, West Conshohocken

Atapour H, Moosavi M (2014) The influence of shearing velocity on shear behavior of artificial joints. Rock Mech Rock Eng 47(5):1745–1761. https://doi.org/10.1007/s00603-013-0481-9

Barbero M, Barla G, Zaninetti A (1996) Dynamic shear strength of rock joints subjected to impulse loading. Int J Rock Mech Min Sci 33(2):141–151. https://doi.org/10.1016/0148-9062(95)00049-6

Bobich JK (2005) Experimental analysis of the extension to shear fracture transition in Berea sandstone. MS thesis, Texas A & M University.

Brace WF (1964) Brittle fracture of rocks. In: Judd WR (ed) State of stress in the earth's crust. American Elsevier, New York, pp 111–180

Cadoni E (2010) Dynamic characterization of orthogenesis rock subjected to intermediate and high strain rates in tension. Rock Mech Rock Eng 43(6):667–676. https://doi.org/10.1007/s00603-010-0101-x

Cai M, Liu D (2009) Study of failure mechanisms of rock under compressive–shear loading using real-time laser holography. Int J Rock Mech Min Sci 46(1):59–68. https://doi.org/10.1016/j.ijrmms.2008.03.010

Cen DF, Huang D (2017) Direct shear tests of sandstone under constant normal tensile stress condition using a simple auxiliary device. Rock Mech Rock Eng 50(6):1425–1438. https://doi.org/10.1007/s00603-017-1179-1

Cen DF, Huang D, Song YX, Jiang QH (2020) Direct tensile behavior of limestone and sandstone with bedding planes at different strain rates. Rock Mech Rock Eng. https://doi.org/10.1007/s00603-020-02070-x

Chen W, Konietzky H, Tan X, Frühwirt T (2016) Pre-failure damage analysis for brittle rocks under triaxial compression. Comput Geotech 74:45–55. https://doi.org/10.1016/j.compgeo.2015.11.018

Cho N, Martin CD, Sego DC (2008) Development of a shear zone in brittle rock subjected to direct shear. Int J Rock Mech Min Sci 45(8):1335–1346. https://doi.org/10.1016/j.ijrmms.2008.01.019

Crawford AM, Curran JH (1981) The influence of shear velocity on the frictional resistance of rock discontinuities. Int J Rock Mech Min Sci Geomech Abstr 18(6):505–515. https://doi.org/10.1016/0148-9062(81)90514-3

Dai F, Huang S, Xia K, Tan Z (2010) Some fundamental issues in dynamic compression and tension tests of rocks using split Hopkinson pressure bar. Rock Mech Rock Eng 43(6):657–666. https://doi.org/10.1007/s00603-010-0091-8

Engelder T (1999) Transitional-tensile fracture propagation: a status report. J Struct Geol 21(8):1049–1055. https://doi.org/10.1016/S0191-8141(99)00023-1

Ferrill DA, Mcginnis RN, Morris AP, Smart KJ (2012) Hybrid failure: field evidence and influence on fault refraction. J Struct Geol 42:140–150. https://doi.org/10.1016/j.jsg.2012.05.012

Frew DJ, Akers SA, Chen W, Green ML (2010) Development of a dynamic triaxial Kolsky bar. Meas Sci Technol 21(10):105704–105713. https://doi.org/10.1088/0957-0233/21/10/105704

Fuenkajorn K, Kenkhunthod N (2010) Influence of loading rate on deformability and compressive strength of three Thai sandstones. Geotech Geol Eng 28(28):707–715. https://doi.org/10.1007/s10706-010-9331-7

Fukui K, Okubo S, Ogawa A (2004) Some aspects of loading-rate dependency of Sanjome andesite strengths. Int J Rock Mech Min Sci 41(7):1215–1219. https://doi.org/10.1016/j.ijrmms.2004.06.001

Gong FQ, Zhao GF (2013) Dynamic indirect tensile strength of sandstone under different loading rates. Rock Mech Rock Eng 47(6):2271–2278. https://doi.org/10.1007/s00603-013-0503-7
Goodman RE (1989) Introduction to rock mechanics, 2nd edn. Wiley, New York, pp 80–83
Haimson B, Bobet A (2012) Introduction to suggested methods for failure criteria. Rock Mech Rock Eng 45(6):973–974. https://doi.org/10.1007/s00603-012-0274-6
Hoek E, Brown ET (1980) Empirical strength criterion for rock masses. J Geotech Eng Div 106(9):1013–1035. https://doi.org/10.1016/0148-9062(81)90766-X
Hoek E, Martin CD (2014) Fracture initiation and propagation in intact rock—a review. J Rock Mech Geotech Eng 6:287–300. https://doi.org/10.1016/j.jrmge.2014.06.001
Huang RQ, Huang D (2014) Evolution of rock cracks under unloading condition. Rock Mech Rock Eng 47(2):453–466. https://doi.org/10.1007/s00603-013-0429-0
Huang D, Zhu TT (2018) Experimental and numerical study on the strength and hybrid fracture of sandstone under tension-shear stress. Eng Fract Mech 200:387–400. https://doi.org/10.1016/j.engfracmech.2018.08.012
Huang D, Zhu TT (2019) Experimental study on the shear mechanical behavior of sandstone under normal tensile stress using a new double-shear testing device. Rock Mech Rock Eng 52:3467–3474. https://doi.org/10.1007/s00603-019-01762-3
Huang RQ, Wang XN, Chan LS (2001) Triaxial unloading test of rocks and its implication for rock burst. Bull Eng Geol Environ 60(1):37–41. https://doi.org/10.1007/s100640000082
Huang S, Feng XT, Xia K (2011) A dynamic punch method to quantify the dynamic shear strength of brittle solids. Rev Sci Instrum 82(5):053901–053905. https://doi.org/10.1063/1.3585983
Huang S, Xia K, Dai F (2012) Establishment of a dynamic Mohr–Coulomb failure criterion for rocks. Int J Nonlin Sci Numer Simul 13(1):55–60. https://doi.org/10.1515/ijnsns.2011.120
Huang D, Li YQ, Song YX, Xu Q, Pei XJ (2019) Insights into the catastrophic Xinmo rock avalanche in Maoxian county, China: combined effects of historical earthquakes and landslide amplification. Eng Geol 258:105158. https://doi.org/10.1016/j.enggeo.2019.105158
Li HB, Zhao J, Li TJ (1999) Triaxial compression tests of a granite at different strain rates and confining pressures. Int J Rock Mech Min Sci 36(8):1057–1063. https://doi.org/10.1016/S1365-1609(99)00120-3
Li H, Li J, Liu B, Li J, Li S, Xia X (2013) Direct tension test for rock material under different strain rates at quasi-static loads. Rock Mech Rock Eng 46(5):1247–1254. https://doi.org/10.1007/s00603-013-0406-7
Li Y, Huang D, Li X (2014) Strain rate dependency of coarse crystal marble under uniaxial compression: strength, deformation and strain energy. Rock Mech Rock Eng 47(4):1153–1164. https://doi.org/10.1007/s00603-013-0472-x
Lin Q, Fakhimi A, Haggerty M, Labuz JF (2009) Initiation of tensile and mixed-mode fracture in sandstone. Int J Rock Mech Min Sci 46(3):489–497. https://doi.org/10.1016/j.ijrmms.2008.10.008
Martin CD, Christiansson R (2009) Estimating the potential for spalling around a deep nuclear waste repository in crystalline rock. Int J Rock Mech Min Sci 46(2):219–228. https://doi.org/10.1016/j.ijrmms.2008.03.001
Nicksiar M, Martin CD (2013) Crack initiation stress in low porosity crystalline and sedimentary rocks. Eng Geol 154:64–76. https://doi.org/10.1016/j.enggeo.2012.12.007
NSPRC GBT50266-2013 (2013) Standard for test methods of engineering rock mass. National Standard of the People's Republic of China **(in Chinese)**
Okubo S, Hashiba K, Fukui K (2013) Loading rate dependency of the strengths of some Japanese rocks. Int J Rock Mech Min Sci 58(1):180–185. https://doi.org/10.1016/j.ijrmms.2012.09.003
Patel S, Martin CD (2018) Application of flattened Brazilian test to investigate rocks under confined extension. Rock Mech Rock Eng 51(4):3719–3736. https://doi.org/10.1007/s00603-018-1559-1
Paterson MS, Wong TF (2005) Experimental rock deformation—the brittle field, 2nd edn. Springer, New York, pp 49–54
Peng J, Rong G, Cai M, Yao M, Zhou C (2016) Comparison of mechanical properties of undamaged and thermal-damaged coarse marbles under triaxial compression. Int J Rock Mech Min Sci 83(4):135–139. https://doi.org/10.1016/j.ijrmms.2015.12.016
Petit JP (1988) Normal stress dependent rupture morphology in direct shear tests on sandstone with applications to some natural fault surface features. Int J Rock Mech Min Sci Geomech Abstr 25(6):411–419. https://doi.org/10.1016/0148-9062(88)90981-3
Ramsey JM, Chester FM (2004) Hybrid fracture and the transition from extension fracture to shear fracture. Nature 428(6978):63–66. https://doi.org/10.1038/nature02333
Ren L, Xie LZ, Xie HP, Ai T, He B (2016) Mixed-mode fracture behavior and related surface topography feature of a typical sandstone. Rock Mech Rock Eng 49(8):3137–3153. https://doi.org/10.1007/s00603-016-0959-3
Rodriguez E (2005) A microstructural study of the extension-to-shear fracture transition in Carrara Marble. MS thesis, Texas A & M University.
Singh TN, Verma AK, Kumar T, Dutt A (2011) Influence of shear velocity on frictional characteristics of rock surface. J Earth Syst Sci 120(1):183–191. https://doi.org/10.1007/s12040-011-0009-1
Tang ZC, Wong LNY (2016) Influences of normal loading rate and shear velocity on the shear behavior of artificial rock joints. Rock Mech Rock Eng 49(6):2165–2172. https://doi.org/10.1007/s00603-015-0822-y
Turichshev A, Hadjigeorgiou J (2016) Triaxial compression experiments on intact veined andesite. Int J Rock Mech Min Sci 86:179–193. https://doi.org/10.1016/j.ijrmms.2016.04.012
USACE (1980) Method of test for direct shear strength of rock core specimens. United States Army Corps of Engineers, Vicksburg
Wang G, Zhang X, Jiang Y, Wu X, Wang S (2016) Rate-dependent mechanical behavior of rough rock joints. Int J Rock Mech Min Sci 83:231–240. https://doi.org/10.1016/j.ijrmms.2015.10.013
Wibberley CAJ, Petit JP, Rives T (2000) Micromechanics of shear rupture and the control of normal stress. J Struct Geol 22(4):411–427. https://doi.org/10.1016/S0191-8141(99)00158-3
Wu F, Liu T, Liu J, Tang X (2009) Excavation unloading destruction phenomena in rock dam foundations. Bull Eng Geol Environ 68(2):257–262. https://doi.org/10.1007/s10064-009-0202-5
Xeidakis GS, Samaras IS, Zacharopoulos DA, Papakaliatakis GE (1997) Trajectories of unstably growing cracks in mixed mode I–II loading of marble beams. Rock Mech Rock Eng 30(1):19–33. https://doi.org/10.1007/BF01020111
Xia K (2013) A Mohr–Coulomb failure criterion for rocks subjected to dynamic loading. In: Yang Q, Zhang J-M, Zheng H, Yao Y (eds) Constitutive modeling of geomaterials. Springer, Berlin, pp 367–370
Xu S, Huang J, Wang P, Zhang C, Zhou L, Hu S (2015) Investigation of rock material under combined compression and shear dynamic loading: an experimental technique. Int J Impact Eng 86(7):206–222. https://doi.org/10.1016/j.ijimpeng.2015.07.014
Yang SQ (2016) Experimental study on deformation, peak strength and crack damage behavior of hollow sandstone under

conventional triaxial compression. Eng Geol 213:11–24. https://doi.org/10.1016/j.enggeo.2016.08.012

Zhang QB, Zhao J (2014) A review of dynamic experimental techniques and mechanical behaviour of rock materials. Rock Mech Rock Eng 47(4):1411–1478. https://doi.org/10.1007/s00603-013-0463-y

Zhao J (2000) Applicability of Mohr–Coulomb and Hoek–Brown strength criteria to the dynamic strength of brittle rock. Int J Rock Mech Min Sci 37(7):1115–1121. https://doi.org/10.1016/S1365-1609(00)00049-6

Zeng B, Huang D, Ye SQ, Chen FY, Zhu TT, Tu YL (2019) Triaxial extension tests on sandstone using a simple auxiliary apparatus. Int J Rock Mech Min Sci 120(2019):29–40. https://doi.org/10.1016/j.ijrmms.2019.06.006